

High-Entropy Intermetallics Serve Ultrastable Single-Atom Pt for Propane Dehydrogenation

Yuki Nakaya, Eigo Hayashida, Hiroyuki Asakura, Satoru Takakusagi, Shunsaku Yasumura, Ken-ichi Shimizu, and Shinya Furukawa*



Cite This: *J. Am. Chem. Soc.* 2022, 144, 15944–15953



Read Online

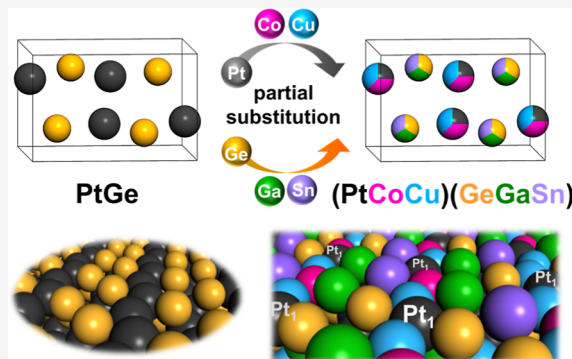
ACCESS |

Metrics & More

Article Recommendations

Supporting Information

ABSTRACT: Propane dehydrogenation has been a promising propylene production process that can compensate for the increasing global demand for propylene. However, Pt-based catalysts with high stability at $\geq 600\text{ }^{\circ}\text{C}$ have barely been reported because the catalysts typically result in short catalyst life owing to side reactions and coke formation. Herein, we report a new class of heterogeneous catalysts using high-entropy intermetallics (HEIs). Pt–Pt ensembles, which cause side reactions, are entirely diluted by the component inert metals in PtGe-type HEIs. The resultant HEI (PtCoCu) $(\text{GeGaSn})/\text{Ca–SiO}_2$ exhibited an outstandingly high catalytic stability, even at $600\text{ }^{\circ}\text{C}$ ($k_{\text{d}}^{-1} = \tau = 4146\text{ }h = 173\text{ d}$), and almost no deactivation of the catalyst was observed for 2 months for the first time. Detailed experimental studies and theoretical calculations demonstrated that the combination of the site-isolation and entropy effects upon multi-metallization of PtGe drastically enhanced the desorption of propylene and the thermal stability, eventually suppressing the side reactions even at high reaction temperatures.



INTRODUCTION

Propylene is one of the most important basic raw materials in the petrochemical industry, which has become increasingly scarce due to the shale gas revolution.^{1–6} On-purpose propylene production *via* selective propane dehydrogenation (PDH) into propylene has been regarded as the most promising propylene production technology compared with other methanol-to-olefins and Fischer–Tropsch-to-olefins because of high propylene selectivity to meet the increasing global demand for propylene. However, due to its endothermicity, PDH requires high operation temperatures ($>600\text{ }^{\circ}\text{C}$) to obtain sufficient propylene yield, in which severe catalyst deactivation by coking and/or sintering inevitably occurs in short periods. In this context, developing an innovative PDH catalyst that exhibits high propylene selectivity and catalyst stability even at $\geq 600\text{ }^{\circ}\text{C}$ is incredibly beneficial for the chemical industry. Although numerous efforts have been made to overcome this obstacle, no outstandingly stable catalyst has yet been found to function for several months without deactivation.

PDH is a structure-insensitive reaction, whereas the undesired side reactions leading to deactivation, such as hydrogenolysis, cracking, and coking, are structure-sensitive.^{1–6} Active metal–metal ensembles such as Pt–Pt sites are known to induce these side reactions. Therefore, the dilution or isolation of Pt–Pt ensembles by an inert metal has been commonly employed as a standard catalyst design

concept for selective and stable PDH.^{1–7} Single-atom alloys (SAAs),⁸ where Pt atoms are isolated by excess counterpart metal such as Cu, are the representative material/approach for this purpose; the undesired propylene decomposition is successfully inhibited over Pt@Cu SAA. However, SAAs typically undergo significant aggregation at $\geq 600\text{ }^{\circ}\text{C}$ due to the insufficient thermal stability, resulting in an irreversible deactivation of the catalyst. Therefore, a novel material that serves isolated Pt with high thermal stability is required to develop an ultrastable catalytic system for PDH. The thermal stability of an alloy can be improved by increasing the number of constituent elements due to the significant contribution of mixing entropy, as observed for high-entropy alloys (HEAs: solid-solution alloys comprising five or more elements with a near-equimolar ratio).^{9–11} Because of the unique characteristics and remarkable performances, the catalytic application of HEAs has received significant attention and amid the “gold rush” in recent years.¹² However, for a random alloy structure, a large excess (>20 equiv) of counterpart metals is needed for the complete isolation of Pt.^{8,13} Therefore, there remain some

Received: January 30, 2022

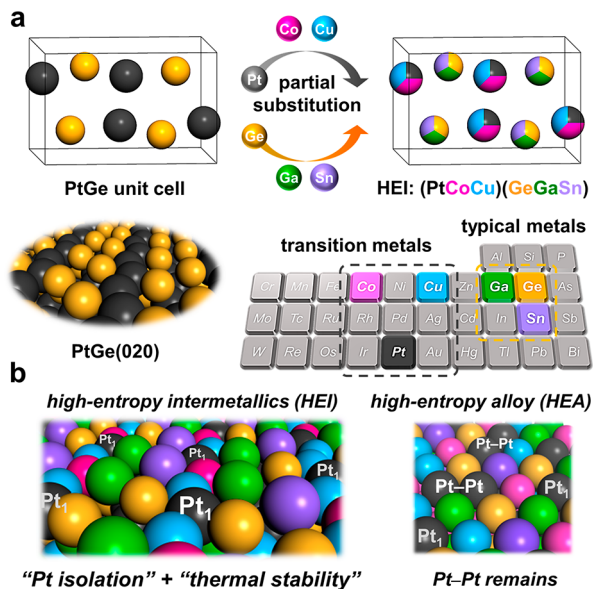
Published: August 19, 2022



Pt–Pt sites in a common (quinary to octonary) HEA. Thus, a multimetallic alloy with a particular ordered structure should be constructed to overcome this challenge.

A possible candidate for such an ideal active site structure is a high-entropy intermetallic (HEI). Unlike HEAs, the constituent metals of an HEI are distributed separately to two (or more) crystallographically distinct sites, depending on the parent intermetallic structure.^{14–18} Scheme 1 illustrates the

Scheme 1. Catalyst Design Concept for Thermally Stable Isolated Pt Site Using the HEI; (a) Pt and Ge Sites in Intermetallic PtGe Are Partially Substituted by Co(Cu) and Ga(Sn), Respectively, Resulting in the Formation of the PtGe-Type HEI (PtCoCu) (GeGaSn) and (b) Illustrations of the (020) Surface of the (PtCoCu) (GeGaSn) HEI (Left) and the (111) Surface of the Pt-Based Senary HEA (Right)



specific catalyst design concept employed in this regard. We focused on PtGe as the parent binary intermetallics (FeAs-type structure, space group: *Pnma*) due to its unique ordered surface structure and significantly negative formation enthalpy ($\Delta H_f = -90.8 \text{ kJ mol}^{-1}$).¹⁹ The former provides one-dimensionally aligned Pt columns separated by Ge columns, where the surface Pt–Pt coordination number is only 2 (Scheme 1a). Besides, the latter can be the driving force to retain the ordered structure upon multi-metallization. Here, the Pt and Ge sites in PtGe are partially substituted by much less active transition (Co and Cu) and inert typical (Ga and Sn) metals, respectively, to form a senary HEI, that is, $(\text{Pt}_x\text{Co}_{0.5-x/2}\text{Cu}_{0.5-x/2})(\text{Ge}_{0.33}\text{Ga}_{0.33}\text{Sn}_{0.33})$ [hereafter, denoted HEI(x)]. These diluent metals were chosen based on the following guidelines: (1) analogous to Pt and Ge (near in the periodic table, Scheme 1a), (2) catalytically less active or inert, and (3) no volatility and toxicity. This site-specific multi-metallization allows the isolation of Pt by Co and Cu and further enhancement in thermal stability by Ga and Sn (see Text S1 for details). Moreover, the degree of Pt isolation can be tuned by changing the Pt fraction x . As a result, the isolated Pt sites surrounded by other inert constituent metals functioned as a highly selective and stable PDH catalyst at high reaction temperatures. This study reports a novel catalyst material and design concept based on HEIs, providing

thermally stable isolated Pt and working as an outstandingly stable catalyst for high-temperature PDH.

RESULTS AND DISCUSSION

The HEI and the related alloy catalysts were prepared by a pore-filling impregnation method as supported nanoparticles using Ca-modified amorphous silica (Ca–SiO₂) (see Tables S1 and S2 for metal loadings and Pt dispersion, respectively). Temperature-programmed reduction by H₂ revealed that all catalysts were fully reduced (Figure S1). The high-angle annular dark field scanning transmission electron microscopy (HAADF-STEM) analysis showed that the nanoparticle size ranged mainly between 1.5 and 3 nm (average: 2.2 nm, Figure S2). Figure 1a shows the elemental maps of a single nanoparticle obtained using the energy-dispersive X-ray analysis, confirming that the nanoparticle comprised Pt, Co, Cu, Ge, Ga, and Sn. Quantitative analysis for some small nanoparticles revealed that the atomic ratios of (Pt + Co + Cu)/(Ge + Ga + Sn) were close to unity (Figure S3). Figure 1b shows the synchrotron X-ray diffraction (XRD) pattern of the HEI(0.25) catalyst, showing a PtGe-type diffraction pattern, unlike fcc- or hcp-type HEAs.¹² The diffraction angles for the HEI were higher than those of the parent PtGe, which can be attributed to lattice shrinkage by substituting Pt with the smaller-size elements, Co and Cu. This experimental lattice shrinkage (5.6%) was well consistent with the theoretical value estimated by Vegard's rule and each atomic radius (5.4%, see Text S2 and Table S3 for details), supporting the formation of the HEI structure. The intensity of 011 diffraction (observed at 9° for PtGe) was lowered for the HEI, which can be attributed to lattice distortion caused by mixing several elements with different atomic radii (see Text S2 for detailed explanation). Such a decrease in the diffraction intensity was also observed in fcc HEA systems.^{20–22}

We also performed X-ray absorption fine structure (XAFS) analysis to obtain further structural information. Figure 1c shows the Pt L_{II}-edge X-ray absorption near-edge structure (XANES) spectra of the Pt/Ca–SiO₂, bulk PtGe, PtGe/Ca–SiO₂, and HEI(0.25) (see Figure S4 for other edges). The bulk PtGe and PtGe/Ca–SiO₂ have diffraction patterns characteristic of intermetallic PtGe (Figures S5 and S6a) and hence can be used as references for bulk and nanoparticulate PtGe, respectively (the nanoparticle size was 1.8 nm on average, Figure S7). HEI(0.25) has a XANES characteristic that was similar to that of bulk PtGe and PtGe/Ca–SiO₂ but different from that of Pt/Ca–SiO₂. In the raw extended XAFS (EXAFS) oscillations, a similar tendency was seen (Figure 1d, see Figure S8 for other edges). Although a small difference in the oscillation feature was observed at $k = 3–6 \text{ \AA}^{-1}$, this can be attributed to the overlap of the Pt–Sn scattering (see also Figure S9, Text S2, and later discussion for details). Notably, the EXAFS oscillation of HEI(0.25) did not match with those of PtGa/Ca–SiO₂ and PtSn/Ca–SiO₂ (Figure S6c), supporting that the HEI retained the PtGe-type crystal structure. Further structural information is presented in the Fourier-transformed EXAFS spectra. Unlike PtGe, HEI(0.25) showed two peaks at 2.0 and 2.5 Å (Figure 1e), which could be assigned to Pt–Ge(Ga) and Pt–Sn scatterings, respectively (Table S4), demonstrating that Sn is doped into the Ge site. Besides, the Pt–Pt scattering at 3.0 Å, observed for PtGe, disappeared upon the multi-metallization. This suggests that Pt atoms were sufficiently isolated by substitution with Co and Cu. We also performed comparable analyses for absorption

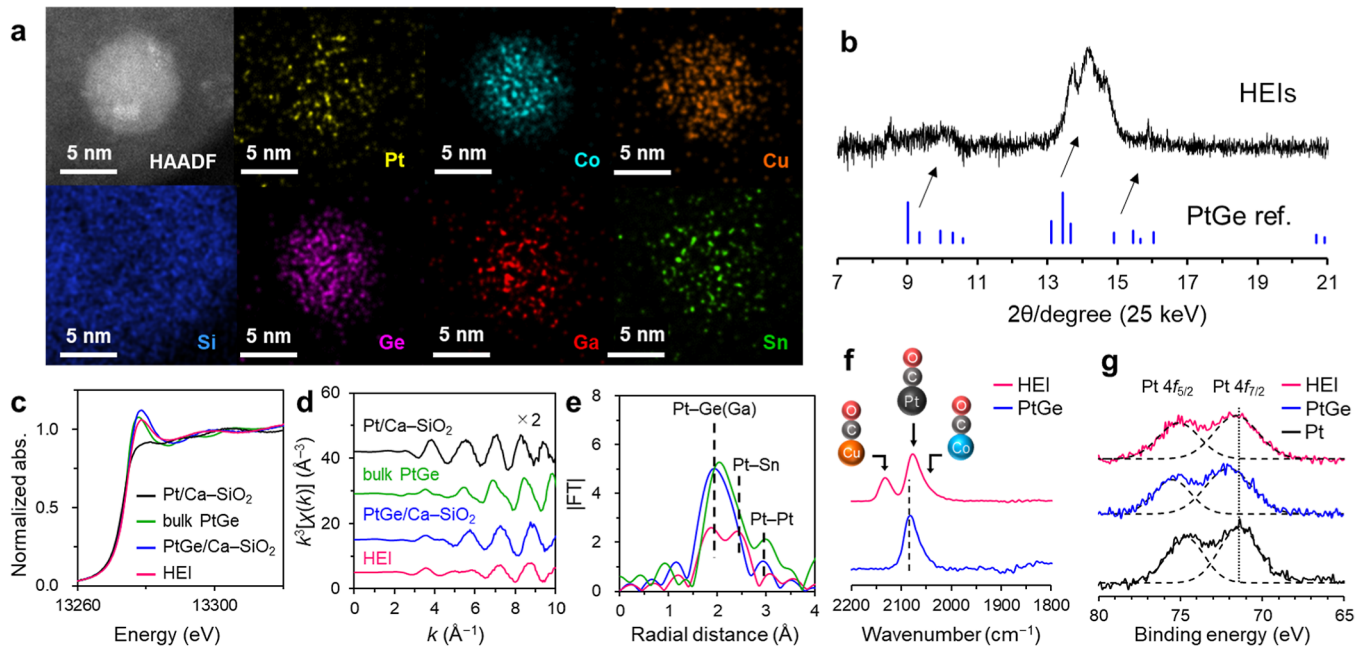


Figure 1. Characterization of the HEI(0.25) catalyst. (a) HAADF-STEM image and the corresponding elemental maps for a single nanoparticle. (b) Synchrotron XRD pattern. Pt L_{II}-edge (c) XANES, (d) k^3 -weighted EXAFS oscillations, and (e) Fourier-transformed EXAFS of Pt/Ca-SiO₂, bulk PtGe, PtGe/Ca-SiO₂, and HEI(0.25). (f) FT-IR spectra of CO adsorbed on PtGe/Ca-SiO₂ and HEI(0.25) at -100 °C. (g) XPS spectra of Pt/Ca-SiO₂, PtGe/Ca-SiO₂, and HEI(0.25).

edges other than Pt L_{II}, where curve fitting allowed us to assign all of the associated transition-typical metal scatterings [e.g., Co–Ge(Ga), Cu–Sn, Ga–Co(Cu), and Sn–Pt, Figure S8 and Table S4; for a more detailed discussion of the EXAFS analysis, see Text S3]. These results comprehensively support the formation of the (PtCoCu)(GeGaSn) HEI structure.

Next, the surfaces of the PtGe and HEI were analyzed by Fourier-transform infrared (FT-IR) spectroscopy with CO adsorption (Figure 1f). The adsorption temperature was set to -100 °C because CO did not adsorb on the HEI at near room temperature (50 °C, Table S2). For PtGe, a peak assigned to linearly adsorbed CO on Pt atoms appeared at 2080 cm⁻¹^{23,24}, which was consistent with the previous study of intermetallic PtGe.²⁵ For HEI(0.25), two kinds of linear CO were observed at 2070 and 2150 cm⁻¹, assignable to those on Pt^{23,24} and Cu,²⁶ respectively. The broad shoulder peak at 2024 cm⁻¹ may be attributed to linear CO on Co.²⁷ For both catalysts, no absorption was observed below 2000 cm⁻¹, indicating the absence of threefold Pt ensembles. These findings are consistent with the substitution of the Pt site in PtGe with Co and Cu. The electronic state of Pt was also investigated using X-ray photoelectron spectroscopy (XPS) analysis (Figure 1g). The Pt 4f_{7/2} binding energy of PtGe (72.1 eV) was higher than that of Pt (71.4 eV), depicting that the electron density of Pt was decreased by alloying with Ge and is consistent with the observation in the literature.^{28,29} On the contrary, the binding energy shifted lower from PtGe to HEI(0.25) (71.6 eV), which suggests that the electron density of the Pt 4f state was slightly recovered upon multi-metallization. Similar trends in the electron density were also observed in the XANES [white line intensity; PtGe > HEI(0.25) > Pt, Figure 1c] and FT-IR studies (frequency of linear CO on Pt; PtGe > HEI, Figure 1f). However, as observed in XANES, the difference in the d-electron density of Pt between PtGe and HEI(0.25) was much smaller than that between PtGe and Pt (Figure 1c). This

indicates that the electronic effect of multi-metallization on the Pt d-state is limited.

We also prepared SAA (Cu–Pt/Ca-SiO₂, Cu/Pt = 25) and quinary HEA (PtFeCoCuGa/Ca-SiO₂) catalysts as control catalysts. The XRD, XAFS (Figures S10 and S11), and HAADF-STEM (Figures S12–S14) analyses confirmed that each catalyst had an fcc structure with high phase purity (see Text S4 for detailed explanation). Moreover, Pt atoms in the SAA were sufficiently isolated (Table S5). Besides, the corresponding quaternary alloys (PtCoCuGe/Ca-SiO₂ and PtCoCuGa/Ca-SiO₂) and binary alloys or intermetallics (PtM/Ca-SiO₂; M = Co, Cu, Ga, Ge, Sn) were prepared. Interestingly, the Ge-containing quaternary alloy had the PtGe-type intermetallic structure, that is, (PtCoCu)Ge (Figures S15 and S16 and Text S5), whereas the Ga-containing one showed an fcc solid-solution phase (Figures S11, S17, and S18 and Text S5). This is probably due to the large difference in ΔH_f between PtGe (-90.8 kJ mol⁻¹)¹⁹ and PtGa (-55.6 kJ mol⁻¹).³⁰ As mentioned for Scheme 1, the significant contribution of the enthalpic term of PtGe seemed to prevail over the entropic effect to form a solid-solution phase upon multi-metallization while that of PtGa did not. This interpretation is also valid to understand the difference between HEI(0.25) and the quinary HEA. A similar characterization was also performed on a series of binary catalysts (Figure S6, Table S5, and Text S6), revealing that the desired bimetallic phases were formed with high phase purities.

We also used an *in situ* XAFS approach to explore the stability of the HEI phase at high temperatures, implying that the original structure of HEI(0.25) was preserved even at 700 °C (Figure S19). Besides, the EXAFS features of the HEI and the fcc HEA were still distinct at 700 °C (Figures S19 and S20). Similar trends were also observed in the XANES region (Figure S21). However, due to the large Debye–Waller factor at the high temperature and the resulting low signal/noise

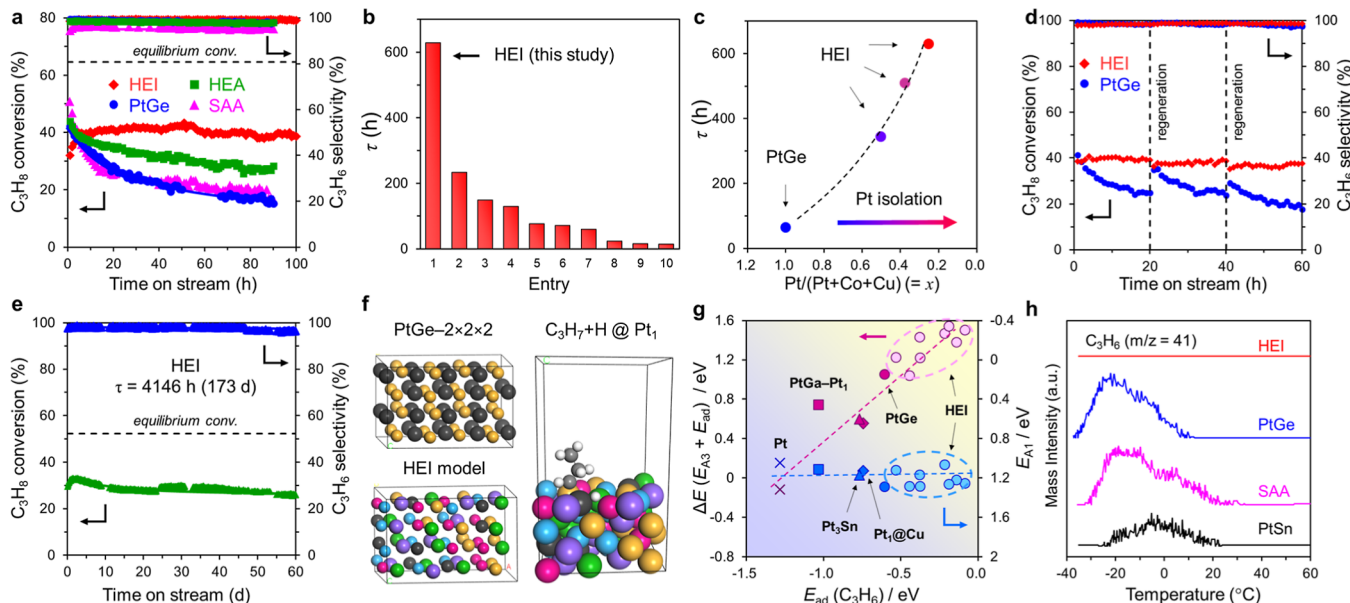


Figure 2. Catalytic performance of the HEI in PDH and DFT calculations. (a) Catalytic performances of the PtGe, HEI(0.25), SAA, and HEA in PDH at 600 °C without co-feeding H₂. (b) Mean catalyst life ($\tau = k_d^{-1}$) of reported catalysts and HEI(0.25) in PDH without co-fed H₂ (references are listed in Tables S8 and S9). (c) Relationship between mean catalyst life ($\tau = k_d^{-1}$) and the degree of Pt isolation represented by x as the Pt/(Pt + Co + Cu) molar ratio in the PtGe and HEI. (d) Reusability of PtGe and HEI(0.25) in PDH at 600 °C after repeated regeneration processes. (e) Long-term stability test of the HEI(0.25) in PDH at 600 °C with co-feeding H₂ (catalyst: 150 mg, C₃H₈/H₂/He = 2.5:1.3:3.7 mL min⁻¹, WHSV = 2.0 h⁻¹). (f) Model structure of the HEI (left bottom) derived from PtGe (left top) for DFT calculations. An example of the HEI slab model for PDH: C₃H₇ + H at a Pt₁ site (right). (g) Relationship between E_{ad} (C₃H₆) and ΔE or E_{A1} for various Pt-based surfaces. (h) C₃H₆-TPD for Pt-based catalysts (adsorption temperature: -35 °C).

ratio, it is difficult to make a definitive conclusion only by XAFS. Therefore, we further conducted ab initio molecular dynamics simulations to confirm the thermal stability of the HEI structure at high temperatures. An HEI structure was modeled and annealed at 25, 600, and 1200 °C (see Text S7 for computational details). Although the initial atomic arrangement and the crystallinity were fully disordered at 1200 °C, they were retained at 600 and at 25 °C (Figures S22 and S23). This strongly supports the thermal stability of the HEI structure at the reaction temperature of PDH. Thus, we successfully synthesized the PtGe-type HEI, which provides thermally stable single-atom Pt as an ideal active site for high-temperature PDH.

Then, we tested the catalytic performances of the prepared catalysts in PDH under a considerably harsh condition (600 °C, without co-feeding H₂). The SAA catalyst and PtGe were deactivated within 20 h (Figure 2a) due to the aggregation of nanoparticles (Figure S12) and coke accumulation (Figure S24 and Table S6), respectively. The quinary HEA (Figure 2a) and quaternary (Figure S25) and binary (Figures S26 and S27) catalysts also showed slow deactivation due to coking (Table S6). Conversely, HEI(0.25) was not deactivated within 100 h (Figure 2a) and retained >30% conversion and 99% propylene selectivity up to 260 h (Figure S28), where the mean catalyst life τ (reciprocal deactivation constant k_d^{-1}) was 628 h (Table S7). Moreover, HEI(0.25) still exhibited good stability at 620 °C (>40% conv. for 120 h, Figure S29). To the best of our knowledge, the HEI catalyst exhibited the highest stability in PDH in the absence of H₂ (Figure 2b, details are listed in Tables S8 and S9), which is highly beneficial for practical application (Text S8). The particle size distribution did not change before and after the 100 h catalytic run (Figures S2 and S30), indicating high thermal stability and strong resistance to

sintering of the HEI, according to the HAADF-STEM analysis. Interestingly, HEI(0.25) showed a short induction period in propane conversion at the initial stage of the reaction (<10 h). Since no change in the bulk structure was observed during this period (see Figure S31 for the XRD patterns), the increase in conversion might be attributed to the change in the Pt/Co/Cu composition ratio at the surface. A possible interpretation is that Pt, Co, and Cu atoms can migrate gradually in the subsurface region under the high-temperature condition; therefore, the Pt/Co/Cu ratio at the surface is gradually optimized by coming in contact with hydrocarbons. We also performed another control experiment using HEI(0.25) without Ca, which resulted in lower stability than that of HEI(0.25) with Ca (Figure S32). Ca is known to act as a spacer for metallic species,³¹ which enhances homogeneous distribution and alloying of metallic species (see Figure S33 for an example of PtSn/Ca-SiO₂), thus promoting sufficient alloying. Therefore, the lower stability may be due to incomplete formation of the HEI structure. Next, we tested HEI(0.375) and HEI(0.5) in PDH, which resulted in lower selectivity and stability (Figure S34 and Table S7). As shown in Figure 2c, a strong positive correlation was observed between the Pt fraction x and the mean catalyst life τ , indicating that the degree of Pt isolation in the HEI determines the selectivity and stability in PDH. Thus, these results demonstrated the validity of our catalyst design concept based on HEIs for high-temperature PDH. Control experiments using the Ca-SiO₂ and unmodified SiO₂ support were also performed at 600 °C, where a small amount of propane was converted to propylene with low selectivity (conv., ~5%; sel., ~60%, Figure S35). This is probably due to a small contribution of noncatalytic thermal cracking.³¹

We subsequently investigated the reusability of the prepared catalysts through repeated regeneration processes (O_2-H_2 treatments, Figure 2d). The catalytic activity of PtGe was recovered after the first regeneration procedure, indicating that this treatment could combust the accumulated coke. However, it was not fully recovered despite repeated regeneration, most likely due to irreversible catalyst decomposition. Conversely, HEI(0.25) showed no deactivation after the repeated regeneration procedures, revealing its high durability in repeated regeneration and reuse. Indeed, the XRD patterns of HEI(0.25) showed no changes after the PDH reaction and regeneration process (Figure S31), indicating that the original crystal structure of HEI(0.25) was retained. Then, the long-term stability of HEI(0.25) was examined in the presence of co-fed H_2 to minimize the coke formation, which is a more common condition for PDH. Notably, HEI(0.25) exhibited outstandingly high stability at 600 °C for the first time; little deactivation was observed for at least 2 months (Figure 2e), where the mean catalyst life ($\tau = 4146$ h) was 1.4 times higher than the highest ever reported ($\tau = 3067$ h) (Tables S10 and S11). Thus, the HEI(0.25) catalyst is the most stable PDH catalyst under different conditions to the best of our knowledge (Figure S36). The coke amount was drastically decreased by co-feeding H_2 (Figure S24) due to the decoking effect of H_2 (coke hydrogenation).³¹ We also focused on the relationship between catalytic activity and stability because a negative correlation between them is often suggested. For this purpose, we calculated the rate constant for the forward direction (k_f) as a universal scale covering the influences of space velocity and the degree of approach to equilibrium (Table S8),^{7,32} which was plotted against the mean catalyst life ($\tau = k_d^{-1}$) for reported Pt-based catalysts (Figure S37). Although a weak negative correlation was observed between activity and stability, HEI(0.25) deviated from this correlation significantly and exceptionally. Therefore, it is unlikely that the outstandingly high stability of the HEI was achieved at the expense of activity but rather due to the combination of site-isolation and entropy effects. However, further increase in the catalytic activity might be required for practical application with efficient propylene productivity.

Finally, we used density functional theory (DFT) computations to ascertain the origin of HEI's exceptional catalytic performance. For PtGe, the (020) plane was considered the main active surface because it is one of the major facets of the PtGe crystal (see Figure S38 and Table S12 for the result of Wulff construction) and much more active for C–H scissions than the most stable (211) and the second stable (112) planes (Figures S39–S48 and Table S13). The HEI(0.25) structure was modeled based on the PtGe–(2 × 2 × 2) supercell, where the Pt and Ge sites were substituted partially and randomly with Co/Cu and Ga/Sn, respectively, such that the Pt fraction x was 0.25 (Figure 2f). Here, we randomly generated 40 structures (Figure S49 and Text S9) and chose the most stable one as an energetically favorable model (Table S14 and Figure S50). The segregation energies of Pt atoms were also calculated for each isolated Pt site, which were mostly positive (Table S15). This indicates that the isolated Pt state is electronically preferable to the segregated state (see Text S10 for details). Then, for slab models, two HEI(040) surfaces [equivalent to the PtGe(020) plane] were considered, each with four distinct isolated Pt atoms and eight Pt–Co/Cu bridge sites for H adsorption (Figure S50). On each Pt–Co/Cu site, the stepwise C–H scissions from C_3H_8

to C_3H_5 were calculated (Figure 2f right, Figures S51–S74, and Table S16). Similar computations were also executed on the (111) surfaces of Pt, Pt₃Sn, and Cu–Pt₁ for comparison (Figures S75–S83 and Table S16, results of PtGa were reproduced from the previous study³³). The third C–H scission triggers propylene decomposition, leading to selectivity decrease, coke formation, and consequent catalyst deactivation (see Scheme S1 and Text S11 for details). Therefore, the propylene selectivity (and catalyst stability) generally depends on the difference in the energy barriers between the third C–H scission and propylene desorption ($\Delta E = E_{A3} - E_d = E_{A3} + E_{ad}$).^{8,33,34} The calculated ΔE were in the following order: Pt (−0.11 eV) ≪ Pt₁@Cu (0.55 eV) ≈ Pt₃Sn (0.60 eV) < Pt₁@PtGa (0.74 eV) < PtGe(020) (1.05 eV) < HEI(040) (1.04 ~ 1.54 eV) (Figure 2g and Table S16), which is consistent with the experimental trend in propylene selectivity (Table S7). Although the ΔE values for the HEI varied depending on the site, they were much higher than those on other bimetallic surfaces, indicating exceptional selectivity and stability. Overall, ΔE linearly increased with the E_{ad} (Figure 2g), indicating that the adsorption strength of propylene on the surface indicates ΔE . Figure 2g also describes that E_{A1} did not vary depending on the surface, consistent with the structure insensitivity of PDH. These results suggest that single-atom Pt on HEIs can selectively catalyze propane's first and second C–H scissions, while effectively inhibiting the third one and subsequent side reactions by facile propylene desorption. Notably, no significant difference was observed in the d-band shapes and centers between PtGe and HEI(0.25) (Figure S84). Therefore, the weakened propylene adsorption can be attributed to a geometric ensemble effect due to the Pt isolation rather than an electronic effect upon multimetalization. We also calculated the d-band structure of Pt–Cu SAA, of which the d-band center was much closer to the Fermi level than those of the PtGe and HEI. This is consistent with the more negative E_{ad} of the SAA (Figure 2g) and the lower propylene selectivity in PDH (Figure 2a).

Guided by the theoretical study outlined above, we conducted temperature-programmed propylene desorption (C_3H_6 -TPD, Figure 2h) with an adsorption temperature of −35 °C (12 °C above the boiling point). The PtGe, PtSn, and Cu–Pt SAA exhibited broad desorption peaks between −40 and 20 °C, where the peak tops appeared in this order. Conversely, no desorption was observed on HEI(0.25), indicating that propylene could not be adsorbed even at −35 °C. This trend agrees with that of E_{ad} and demonstrates the remarkably easy desorption of propylene from the HEI. We also used CO-TPD, which revealed a similar pattern (Figure S85). As a result, the Pt isolation using HEIs allows for months of selective and continuous propylene production via PDH.

On the other hand, the DFT model considered in this study was the bulk and slab structures but not a nanoparticle on an oxide support. Considering the small size and the interaction with the silica support, the trends in selectivity and thermal stability may be influenced by the nanosizing and support effects. To obtain the insights closer into the real HEI/SiO₂ catalyst, more sophisticated theoretical studies based on a supported nanoparticle model are preferred.^{35–39} Although modeling and studying such a complex system are highly challenging, success in this approach will advance the chemistry of HEI-based catalysis.

CONCLUSIONS

In the present study, we designed the PtGe-type HEIs to construct thermally stable single-atom Pt sites for PDH. The Pt and Ge sites of intermetallic PtGe were substituted with Co/Cu and Ga/Sn, respectively, which formed the nanoparticulate (PtCoCu)(GeGaSn) HEI on the Ca–SiO₂ support. The degree of Pt isolation can be tuned by the Pt fraction in the Pt site [Pt/(Pt + Co + Cu) ratio], in which Pt atoms are sufficiently isolated at a ratio of 0.25. The single-atom-like Pt sites in HEI(0.25) effectively promote the desorption of as-generated propylene to inhibit undesired side reactions. The HEI(0.25) catalyst is capable of working in PDH at 600 °C for at least 2 months for the first time.

The role of each metal element is summarized as follows: (1) Pt works as the main active metal for C–H activation. (2) Ge, which is catalytically inactive, is the parent counterpart metal that determines the intermetallic PtGe structure and reduces the surface Pt–Pt coordination number to 2. (3) Less active Co and Cu further dilute the Pt–Pt bridge sites in the transition metal site of the HEI and provide isolated Pt sites. (4) Ga and Sn partially substitute the Ge site, which does not directly affect the catalysis, while increasing the thermal stability of the HEI phase due to the entropy effect. (5) Ca works as a spacer to enhance the metal dispersion and alloying.

Thus, the multi-metallization strategy based on HEIs is an ideal design concept for thermally stable single-atom Pt sites for light alkane activation.

METHODS

Catalyst Preparation. (PtCoCu)(GeGaSn)/Ca–SiO₂, namely, HEI(0.25), was synthesized by the pore-filling co-impregnation method, which can deposit all the metal components on the SiO₂ support without loss.⁴⁰ Pt(NH₃)₂(NO₃)₂ (Furuya Metal Co. Ltd., 4.60 wt % of Pt in HNO₃ solution), Co(NO₃)₂·6H₂O (Wako, ≥98.0%), Cu(NO₃)₂·3H₂O (Sigma-Aldrich, ≥99%), (NH₄)₂GeF₆ (Alfa Aesar, 99.99%), Ga(NO₃)₃·nH₂O (*n* = 7–9, Wako, 99.9%), (NH₄)₂SnCl₆ (Alfa Aesar, 98%), and Ca(NO₃)₂·4H₂O (Wako, 98.5%) were used as precursors. The loading amount of Pt was fixed at 1 wt %. The detailed molar ratios of metals are given in Table S1. Mixed aqueous solution of the metal precursors was first added dropwise to SiO₂ (CARIACT G-6, Fuji Silysia, S_{BET} = ca. 500 m² g⁻¹) so that the solutions just filled the pore of SiO₂ (ca. 1.6 mL of solution per g of SiO₂). The obtained mixtures were sealed using three pieces of a plastic film and kept overnight at room temperature, followed by transferring to a round-bottom flask and subsequent freezing using liquid nitrogen. The frozen mixtures were dried in vacuum at ca. -5 °C and further dried in an oven at 90 °C overnight. The resulting powder was calcined at 400 °C for 1 h in dry air with a ramping rate of 1 °C min⁻¹. The calcined powder was then reduced under flowing H₂ (0.1 MPa, 50 mL min⁻¹) at 700 °C for 1 h with a ramping rate of 20 °C min⁻¹. The metal content of HEI(0.25) was estimated using inductively coupled plasma atomic emission spectroscopy (ICP-AES) as follows: Pt: 0.96 wt %, Co: 0.45 wt %, Cu: 0.53, Ge: 0.44 wt %, Ga: 0.53 wt %, Sn: 0.89 wt %, and Ca: 3.01 wt %, which were close to the fed compositions (Pt: 1.00 wt %, Co: 0.45 wt %, Cu: 0.49, Ge: 0.56 wt %, Ga: 0.71 wt %, Sn: 0.91 wt %, and Ca: 3.08 wt %).

PtFeCoCuGa/Ca–SiO₂ (HEA), (PtCoCu)Ge/Ca–SiO₂, and PtCoCuGa/Ca–SiO₂ catalysts were also prepared in a similar method to that of the HEI. The loading amount of Pt was fixed at 1 wt %. The detailed molar ratios of metals are summarized in Table S1. Fe(NO₃)₃·6H₂O (Sigma-Aldrich, ≥98%) was used as a precursor for the HEA.

Pt_{0.5}M_{0.5}/Ca–SiO₂ (solid solution alloys, M = Co and Cu) and PtM'/Ca–SiO₂ (intermetallic compounds, M' = Ge, Ga, and Sn) catalysts were also prepared in a similar method to that of the HEI.

The loading amount of Pt was fixed at 1 wt %. The detailed molar ratios of metals are summarized in Table S1.

The Pt–Cu/Ca–SiO₂, namely, SAA, catalyst was also prepared in a similar method to that of the HEI. The loading of Pt and the ratio of Cu/Pt were fixed at 1 and 25 wt %, respectively. Pt–Cu/Ca–SiO₂ catalysts with different Cu/Pt ratios were also prepared in a similar method to that of the SAA catalyst (see Table S1 for the detailed atomic ratio).

Bulk PtGe powder was synthesized by mixing aqueous solutions of Pt(NH₄)₄(OH)_{2(aq)} and (NH₄)₂GeF_{6(aq)}. First, an aqueous solution (total 4.0 g) containing 114.2 mg of (NH₄)₂GeF₆ (Thermo Scientific, 99.99%) was added dropwise to a vigorously stirred aqueous solution of Pt(NH₄)₄(OH)_{2(aq)} (4.87 g, Furuya Metal, Pt: 2.05 wt %), followed by stirring for 30 min. Then, the precipitate was corrected by centrifugation and washed with water three times. The resultant mixture was dried in an oven at 90 °C overnight, followed by reduction under flowing H₂ (0.1 MPa, 50 mL min⁻¹) at 700 °C for 1 h with a ramping rate of 20 °C min⁻¹.

Catalyst Reaction. The PDH reactions were performed in a vertical, quartz fixed-bed reactor with an internal diameter of 4 mm under an atmospheric pressure. Typically, 20–100 mg of catalysts was charged in the reactor. Prior to the catalytic test, the catalyst was reduced under flowing H₂ at 600 °C for 0.5 h, and the reactant gas mixture was subsequently fed, C₃H₈/He = 2.5:5.0, a total of 7.5 mL min⁻¹ (WHSV = 3.0–14.8 h⁻¹). Weight hourly space velocity (WHSV) was calculated based on the weight of C₃H₈ and the catalyst. For the long-term stability tests of the HEI catalyst at 600 °C with co-feeding H₂, 150 mg of the catalyst was used to obtain over 30% propane conversion (WHSV = 2.0 h⁻¹). Prior to the catalytic test, the catalyst was pretreated under flowing H₂ (10 mL min⁻¹) at 600 °C for 0.5 h, and the reactant gas mixture was subsequently fed, C₃H₈/H₂/He = 2.5:1.3:3.7, a total of 7.5 mL min⁻¹. During the long-term reaction, the propane source was almost run out (TOS of 24 d); therefore, we changed it to a new one. The pressure of propane upstream was slightly changed at that time, which seemed to cause the temporal jump in propane conversion. However, the conversion jump was eventually resolved over time (Figure 2a). The product gas was analyzed by online gas chromatography-equipped downstream with a thermal conductivity detector (TCD; Shimadzu GC-8A) and a column of Gaskuropak S4 (GL Science). For all the catalysts, C₃H₈, C₂H₄, C₂H₆, and CH₄ were detected as reaction products. C₃H₈ conversion, C₃H₆ selectivity, C₃H₈ yield, and material balance were defined using eqs 1–4, respectively. Material balance typically ranged between 98 and 102% for all the reactions.

$$\text{C}_3\text{H}_8 \text{ conversion (\%)} = \frac{[\text{C}_3\text{H}_8]_{\text{inlet}} - [\text{C}_3\text{H}_8]_{\text{outlet}}}{[\text{C}_3\text{H}_8]_{\text{inlet}}} \times 100 \quad (1)$$

$$\text{C}_3\text{H}_6 \text{ selectivity (\%)} = \frac{[\text{C}_3\text{H}_6]}{[\text{C}_3\text{H}_6] + \frac{2}{3}[\text{C}_2\text{H}_6] + \frac{2}{3}[\text{C}_2\text{H}_4] + \frac{1}{3}[\text{CH}_4]} \times 100 \quad (2)$$

$$\text{C}_3\text{H}_6 \text{ yield (\%)} = \frac{[\text{C}_3\text{H}_6]_{\text{outlet}}}{[\text{C}_3\text{H}_8]_{\text{inlet}}} \times 100 \quad (3)$$

$$\begin{aligned} \text{Material balance (\%)} &= \frac{[\text{C}_3\text{H}_8]_{\text{outlet}} + [\text{C}_3\text{H}_6] + \frac{2}{3}[\text{C}_2\text{H}_6] + \frac{2}{3}[\text{C}_2\text{H}_4] + \frac{1}{3}[\text{CH}_4]}{[\text{C}_3\text{H}_8]_{\text{inlet}}} \\ &\times 100 \end{aligned} \quad (4)$$

To estimate the catalyst stability, the first-order deactivation model was employed.¹ k_d (h⁻¹) and τ (h) were defined using eqs 5 and 6, respectively. k_d (h⁻¹) and τ (h) represent the deactivation rate constant and mean catalyst life, respectively. Here, lower k_d and higher τ values represent higher catalyst stability.

$$k_d = \frac{\ln\left(\frac{1 - conv_{end}}{conv_{start}}\right) - \ln\left(\frac{1 - conv_{start}}{conv_{start}}\right)}{t} \quad (5)$$

$$\tau = \frac{1}{k_d} \quad (6)$$

where $conv_{start}$ and $conv_{end}$ indicate the initial and final C_3H_8 conversion, respectively. t indicates time on stream. The rate constant for the forward direction (k_f) of PDH was estimated using eq 7.

$$k_f = \frac{R}{P_{C_3H_8}\left(1 - \frac{1}{K_e} \frac{P_{C_3H_8} P_{H_2}}{P_{C_3H_8}}\right)} \quad (7)$$

where R , P_X , and K_e are the specific activity [$\text{mol}_{C_3H_8} \text{ g}_{\text{Pt}}^{-1} \text{ h}^{-1}$], partial pressure of X [bar], and the equilibrium constant [bar], respectively.^{7,32}

Regeneration Process. After the PDH reaction, a spent catalyst was cooled to room temperature under flowing He (25 mL min⁻¹). Then, the catalyst was calcined at 450 °C for 1 h under flowing 20% O_2/He (25 mL min⁻¹) with a ramping rate of 20 °C min⁻¹ and then cooled to room temperature. Afterward, the catalyst was purged under He (25 mL min⁻¹) and subsequently reduced at 700 °C for 1 h under flowing H_2 (10 mL min⁻¹) with a ramping rate of 20 °C min⁻¹.

Characterizations. The crystalline phase in the prepared catalysts was analyzed in an *ex situ* mode using powder XRD (Rigaku, MiniFlex 700+D/teX Ultra; Cu K α X-ray source).

Synchrotron XRD measurement was carried out for the HEI catalyst at BL19B2 beamlines of SPring-8, Japan Synchrotron Radiation Research Institute (JASRI). A wavelength of 0.5 Å (25 keV) was utilized as the X-ray source.

HAADF-STEM was used to investigate the particle size distribution and the crystal structure of the prepared catalyst using an FEI Titan G2 microscope equipped with an energy-dispersive X-ray analyzer operated at 300 kV. Prior to the observation, the as-reduced catalyst was first ground and dispersed in ethanol by ultrasonication. Then, the dispersed catalyst was deposited on a molybdenum grid and dried in vacuum. The particle size distribution was estimated by using length mean particle size.

H_2 temperature-programed reduction (H_2 -TPR) was performed using a BELCAT-II (Microtrac BEL) instrument. Prior to the H_2 -TPR, 30 mg of the as-calcined (not reduced) catalyst was heated under a flow of Ar (20 mL min⁻¹) at 300 °C for 30 min to remove the physically absorbed species (such as H_2O). Then, the catalyst was cooled to 100 °C and subsequently heated from 100 to 900 °C with a ramping rate of 2 °C min⁻¹ under a flow of 5% H_2/Ar (20 mL min⁻¹). The H_2 consumption was quantified using a TCD equipped downstream in BELCAT-II.

The dispersion of Pt in the catalyst was estimated by CO-pulse chemisorption at -100 °C using the BELCAT-II (Microtrac BEL) instrument. Prior to chemisorption, 100 mg of the catalyst was reduced under a 5% H_2/Ar flow (20 mL min⁻¹) at 600 °C for 30 min and then cooled to -100 °C using CATCryo-II under a He flow (20 mL min⁻¹). Afterward, a pulse of 10% CO/He was introduced into the reactor, and CO passed through the catalyst bed was quantified using a TCD equipped downstream. This CO pulse introduction was repeated until the TCD signal remained unchanged due to the effluent CO gas (the amount of chemisorbed CO reached saturation). For the calculation of Pt dispersion, the stoichiometry of chemisorbed CO/Pt was estimated as 1.

The FT-IR spectra of adsorbed CO were obtained using a JASCO FTIR-4100 spectrometer with a mercury–cadmium–telluride (MCT) detector in a transmission mode (resolution 4 cm⁻¹) under a dynamic condition. Prior to CO chemisorption, 100 mg of the catalyst was pressed into a pellet (diameter: 20 mm) and placed in a pretreatment room (quartz). The catalyst was heated to 600 °C and kept at the same temperature under flowing H_2 at 600 °C for 1 h. The reduced sample was then evacuated in vacuum at 600 °C for 1 h, cooled to room temperature, and subsequently transferred to a

measurement room, equipped with CaF₂ windows and a vessel, without exposure to air. Then, the sample was cooled to ca. -100 °C using cooled ethanol. The sample was subsequently exposed to 10% CO/He flow and then evacuated in vacuum to remove CO in the gas phase and physisorbed on the catalyst. During the measurement, the infrared ray was cut by 20% using a filter.

XPS analysis was performed using a JEOL JPS-9010MC spectrometer (X-ray source: Mg K α radiation). First, the as-reduced catalysts were re-reduced at 700 °C for 30 min under flowing H_2 (50 mL min⁻¹), then cooled to room temperature, and subsequently transferred into an Ar glovebox (O_2 : <0.1 ppm) without exposing to air. Afterward, the catalysts were loaded on carbon tape and transferred into the spectrometer using the transfer vessel without air exposure. The obtained spectra were calibrated with the Si 2p emission of the SiO_2 support (103.9 eV).

The amount of coke accumulated on the spent catalysts after PDH was quantified by temperature-programed oxidation (TPO). First, 60 mg of the fresh catalyst (Pt 1 wt %) was used for PDH at 600 °C for 20 h. Then, the spent catalyst (30 mg) was transferred into a quartz tube reactor. Prior to the TPO experiment, the catalyst was first pretreated at 300 °C for 0.5 h under flowing He (10 mL min⁻¹), then cooled to 100 °C, subsequently heated from 100 to 700 °C with a ramping rate of 2 °C min⁻¹ under flowing 2% O_2/He (50 mL min⁻¹), and kept at 700 °C for 10 min. The outlet gas (typically CO_2 ; m/z = 44) was analyzed online using a quadrupole mass spectrometer (BELMASS) equipped downstream.

C_3H_6 temperature-programed desorption (C_3H_6 -TPD) was carried out using a BELCAT-II (Microtrac BEL) instrument. Prior to the C_3H_6 -TPD, the as-reduced catalyst (100 mg) was heated to 600°C under a 5% H_2/Ar gas mixture (20 mL min⁻¹) with a ramping rate of 20 °C min⁻¹ and then kept at the same temperature for 0.5 h. After the reduction, the catalyst was cooled to -35 °C using CATCryo-II under a He flow (20 mL min⁻¹), then kept at -35 °C for 0.5 h, and subsequently exposed to a 5% C_3H_6/He gas mixture (20 mL min⁻¹) at the same temperature for 5 min. The catalyst was then purged under He (50 mL min⁻¹) at -35 °C for 1.5 h and subsequently heated from -35 to 300 °C with a ramping rate of 2 °C min⁻¹. The outlet gas (C_3H_6 ; m/z = 41) was analyzed online using a quadrupole mass spectrometer (BELMASS) equipped downstream.

CO-TPD was performed using a JASCO FTIR-4100 spectrometer with an MCT detector in a transmission mode (resolution 4 cm⁻¹) under a dynamic condition. First, 100 mg of the catalyst was pressed into a pellet (diameter: 20 mm) and placed in a measurement room (Pyrex). The catalyst was then heated to 500 °C with a ramping rate of 20 °C min⁻¹ and kept at the same temperature under flowing 15% H_2/He (70 mL min⁻¹). After the reduction, the sample was cooled to room temperature and subsequently purged under He (60 mL min⁻¹) for 10 min. Afterward, the sample was exposed to 10% CO/He flow for 10 min, then purged under He (60 mL min⁻¹) to remove CO in the gas phase, and physisorbed on the catalyst. Finally, the sample was heated with a ramping rate of 10 °C min⁻¹. During the measurement, the infrared ray was cut by 20% using a filter.

The actual metal content of HEI(0.25) was measured using ICP-AES at the Instrumental Analysis Division, Global Facility Center, Creative Research Institution, Hokkaido University.

XAFS measurements of the catalysts and reference samples were carried out at BL01B1 and BL14B2 beamlines of SPring-8, JASRI. XAFS spectra were recorded at the Pt L_{II}- and Co K-, Cu K-, Ge K-, Ga K-, and Sn K-edges in the transmission mode at room temperature using a Si(111) double-crystal monochromator. Typically, XAFS spectra for the Pt-containing catalyst are recorded at the Pt L_{III}-edge. However, Ge K-edge oscillation interfered with the Pt L_{III}-edge XAFS spectra; therefore, Pt L_{II}-edge spectra were chosen in this study. Besides, the Pt L_{III}- and Pt L_I-edge oscillations also interfere with the Ge K-edge and Pt L_{II}-edge spectra, respectively. Therefore, the XAFS oscillations for Pt L_{II}- and Ge K-edges at high k values (>ca. 11) do not provide the important information for structural analysis due to the overlap of the adjacent XANES spectra. Prior to pelletization, the catalyst was crushed using an agate mortar for more than 40 min to suppress the hole effect. Then, the crushed catalyst was pressed into a

pellet (diameter of 7 mm). For *in situ* XAFS measurement, the pelletized sample of the as-calcined (not reduced) catalyst was transferred into a quartz cell and pre-reduced at 700 °C for 60 min under flowing 50% H₂/He (50 mL min⁻¹) and then cooled to room temperature under He gas flow (25 mL min⁻¹). For *ex situ* XAFS measurement, the pelletized sample of the as-reduced catalyst was transferred into a quartz cell and pre-reduced at 700 °C for 30 min (bulk PtGe: 650 °C for 1 h) under flowing H₂ (50 mL min⁻¹) and then cooled to room temperature. After the pretreatment, the quartz tube containing the reduced pellet was sealed and transferred into an Ar glovebox (O₂: <0.1 ppm) without exposing to air. The pellet was sealed in a plastic film bag (Barrier Nylon) together with an oxygen absorber (ISO A500-HS: Fe powder). The spectra were recorded several times and merged at each measurement step to obtain a good signal-to-noise (S/N) ratio. The obtained XAFS spectra were analyzed using Athena and Artemis software ver. 0.9.25 implemented in the Demeter package.⁴¹ The back-scattering amplitude and phase shift functions were calculated using FEFF8.⁴² The R-factor (R^2) for curve fitting was defined as follows: $R^2 = \sum_i \{k^3 \chi_i^{\text{exp}}(k) - k^3 \chi_i^{\text{fit}}(k)\}^2 / \sum_i \{k^3 \chi_i^{\text{exp}}(k)\}^2$.

DFT Calculations. Periodic DFT calculations were performed using the CASTEP code⁴³ with Vanderbilt-type ultrasoft pseudopotentials and the revised version of the Perdew–Burke–Ernzerhof exchange–correlation functional based on the generalized gradient approximation.⁴⁴ The plane-wave basis set was truncated at a kinetic energy of 360 eV. A Fermi smearing of 0.1 eV was utilized. Dispersion correlations were considered using the Tkatchenko–Scheffler method with a scaling coefficient of $s_R = 0.94$ and a damping parameter of $d = 20$.⁴⁵ The reciprocal space was sampled using a k -point mesh with a spacing of typically 0.04 Å⁻¹, as generated by the Monkhorst–Pack scheme.⁴⁶ Geometry optimizations were performed on supercell structures using periodic boundary conditions. The surfaces were modeled with a thickness of four atomic layers with 13 Å of vacuum spacing. The unit cell size of the bulk crystal was first optimized, followed by modeling the slab structure and surface relaxation with the size of the supercell fixed. The convergence criteria for structure optimization and energy calculation were set to (a) an self-consistent field (SCF) tolerance of 1.0×10^{-6} eV per atom, (b) an energy tolerance of 1.0×10^{-5} eV per atom, (c) a maximum force tolerance of 0.05 eV Å⁻¹, and (d) a maximum displacement tolerance of 1.0×10^{-3} Å. For all calculations, the net charge was set to 0, and spin polarization was considered. The adsorption energy was defined as follows: $E_{\text{ad}} = E_{\text{A-S}} - (E_{\text{S}} + E_{\text{A}})$, where $E_{\text{A-S}}$ is the energy of the slab together with the adsorbate, E_{A} is the total energy of the free adsorbate, and E_{S} is the total energy of the bare slab. Surface energy calculations were conducted for densely packed low-index planes of PtGe such as (211), (202), (112), (002), (020), (102), and (103). The surface energy was defined as follows: $\gamma = (E_{\text{S}} - NE_{\text{B}})/2A$, where E_{B} is the energy of the bulk unit cell, A is the surface area, and N is the number of unit cells in the slab. Transition state search was carried out based on the complete linear synchronous transit/quadratic synchronous transit method^{47,48} with a tolerance for all root-mean-square forces on an atom of 0.10 eV Å⁻¹.

For constructing the HEI(0.25) structure, a PtGe-(2 × 2 × 2) supercell was considered as a base structure. Some Pt and Ge atoms in the supercell were substituted with Co/Cu and Ga/Sn atoms, respectively, so that the Pt/(Pt + Co + Cu) and Ge/(Ga + Ge + Sn) ratios were 0.25 and 0.33, respectively (total numbers; Pt: 8, Co: 12, Cu: 12, Ga: 11, Ge: 11, and Sn: 10). The configuration of each element (Pt, Co, and Cu in the Pt sites and Ga, Ge, and Sn in the Ge sites) was randomly determined using the RAND and RANK functions in Excel. Besides, the following restrictions were employed to maximize the configuration entropy, which cannot be considered by conventional DFT and is expected to be thermodynamically likely: (1) all the Pt atoms in each (040) plane are isolated (no Pt–Pt), and (2) the number of each element in each (040) plane is almost the same (Pt: 2, Co: 3, Cu: 3, Ga: 2 or 3, Ge: 2 or 3, and Sn: 2 or 3) (mode A). In addition, purely random distributions without these restrictions were also considered (mode B). We generated 40 (20 for modes A and B) configurations that were geometrically optimized and

chose the most energetically stable one as a likely structure (Figures S49 and S50, Text S9, and Table S14). The first [HEI(040):A] and the second [HEI(040):B] top layers of the (040) plane of the supercell were selected as the model surfaces of HEI(0.25) (Figure S50). There are four isolated Pt atoms and eight Pt–Co(Cu) bridge sites (A1–A4 and B1–B4) as the H adsorption sites. The stepwise C–H scissions of propane were considered for the eight different active sites so that the eliminated hydrogen atom was captured by the bridge site, whereas the carbon moiety was placed on the Pt atom (Figures S51–S74 and Table S16).

ASSOCIATED CONTENT

Supporting Information

The Supporting Information is available free of charge at <https://pubs.acs.org/doi/10.1021/jacs.2c01200>.

Details on XAFS, XRD, HAADF-STEM, DFT, catalytic test, and additional explanations (PDF)

AUTHOR INFORMATION

Corresponding Author

Shinya Furukawa – Institute for Catalysis, Hokkaido University, Sapporo 001-0021, Japan; Elements Strategy Initiative for Catalysts and Batteries, Kyoto University, Kyoto 615-8520, Japan; Precursory Research for Embryonic Science and Technology, Japan Science and Technology Agency, Tokyo 102-0076, Japan;  orcid.org/0000-0002-2621-6139; Email: furukawa@cat.hokudai.ac.jp

Authors

Yuki Nakaya – Institute for Catalysis, Hokkaido University, Sapporo 001-0021, Japan;  orcid.org/0000-0001-8457-1369

Eigo Hayashida – Institute for Catalysis, Hokkaido University, Sapporo 001-0021, Japan

Hiroyuki Asakura – Elements Strategy Initiative for Catalysts and Batteries, Kyoto University, Kyoto 615-8520, Japan

Satoru Takakusagi – Institute for Catalysis, Hokkaido University, Sapporo 001-0021, Japan;  orcid.org/0000-0002-4095-172X

Shunsaku Yasumura – Institute for Catalysis, Hokkaido University, Sapporo 001-0021, Japan;  orcid.org/0000-0002-4951-186X

Ken-ichi Shimizu – Institute for Catalysis, Hokkaido University, Sapporo 001-0021, Japan; Elements Strategy Initiative for Catalysts and Batteries, Kyoto University, Kyoto 615-8520, Japan;  orcid.org/0000-0003-0501-0294

Complete contact information is available at: <https://pubs.acs.org/doi/10.1021/jacs.2c01200>

Funding

This work was supported by JSPS KAKENHI (grant numbers 17H04965, 20H02517, and 21J20594), the MEXT project Element Strategy Initiative (JPMXP0112101003), JST PRESTO (JPMJPR19T7), and JST CREST (JPMJCR17J3).

Notes

The authors declare no competing financial interest.

ACKNOWLEDGMENTS

The XAFS analysis was performed at the BL01B1 (nos. 2020A0611, 2021A1387, 2021A1571, and 2021B1795) and BL14B2 (2021A1541) beamlines of SPring-8 at the Japan Synchrotron Radiation Research Institute (JASRI). The XAFS analysis for bulk PtGe was carried out at the BL-9A (no.

2020G643) of the Photon Factory at KEK. Synchrotron XRD was carried out at the BL19B2 (2021A2023) beamlines of SPring-8 at JASRI. We appreciate the technical staff of the faculty of engineering and Kah Wei Ting, Hokkaido University, for help with HAADF-STEM observation and XPS measurement, respectively. We thank the Instrumental Analysis Division, Global Facility Center, Creative Research Institution, Hokkaido University, for ICP–AES analysis and providing insights and expertise that greatly assisted the research.

■ REFERENCES

- (1) Sattler, J. J. H. B.; Ruiz-Martinez, J.; Santillan-Jimenez, E.; Weckhuysen, B. M. Catalytic Dehydrogenation of Light Alkanes on Metals and Metal Oxides. *Chem. Rev.* **2014**, *114*, 10613–10653.
- (2) Hu, Z. P.; Yang, D.; Wang, Z.; Yuan, Z. Y. State-of-the-Art Catalysts for Direct Dehydrogenation of Propane to Propylene. *Chin. J. Catal.* **2019**, *40*, 1233–1254.
- (3) Chen, S.; Pei, C.; Sun, G.; Zhao, Z.-J.; Gong, J. Nanostructured Catalysts toward Efficient Propane Dehydrogenation. *Acc. Mater. Res.* **2020**, *1*, 30–40.
- (4) Wang, G.; Zhu, X.; Li, C. Recent Progress in Commercial and Novel Catalysts for Catalytic Dehydrogenation of Light Alkanes. *Chem. Rec.* **2020**, *20*, 604–616.
- (5) Liu, S.; Zhang, B.; Liu, G. Metal-Based Catalysts for the Non-Oxidative Dehydrogenation of Light Alkanes to Light Olefins. *React. Chem. Eng.* **2021**, *6*, 9.
- (6) Chen, S.; Chang, X.; Sun, G.; Zhang, T.; Xu, Y.; Wang, Y.; Pei, C.; Gong, J. Propane Dehydrogenation: Catalyst Development, New Chemistry, and Emerging Technologies. *Chem. Soc. Rev.* **2021**, *50*, 3315–3354.
- (7) Motagamwala, A. H.; Almallahi, R.; Wortman, J.; Igenegbai, V. O.; Linic, S. Stable and Selective Catalysts for Propane Dehydrogenation Operating at Thermodynamic Limit. *Science* **2021**, *373*, 217–222.
- (8) Sun, G.; Zhao, Z. J.; Mu, R.; Zha, S.; Li, L.; Chen, S.; Zang, K.; Luo, J.; Li, Z.; Purdy, S. C.; Kropf, A. J.; Miller, J. T.; Zeng, L.; Gong, J. Breaking the Scaling Relationship via Thermally Stable Pt/Cu Single Atom Alloys for Catalytic Dehydrogenation. *Nat. Commun.* **2018**, *9*, 4454.
- (9) Yeh, J. W.; Chen, S. K.; Lin, S. J.; Gan, J. Y.; Chin, T. S.; Shun, T. T.; Tsau, C. H.; Chang, S. Y. Nanostructured High-Entropy Alloys with Multiple Principal Elements: Novel Alloy Design Concepts and Outcomes. *Adv. Eng. Mater.* **2004**, *6*, 299–303.
- (10) Cantor, B.; Chang, I. T. H.; Knight, P.; Vincent, A. J. B. Microstructural Development in Equiatomic Multicomponent Alloys. *Mater. Sci. Eng. A* **2004**, *375–377*, 213–218.
- (11) George, E. P.; Curtin, W. A.; Tasan, C. C. High Entropy Alloys: A Focused Review of Mechanical Properties and Deformation Mechanisms. *Acta Mater.* **2020**, *188*, 435–474.
- (12) Xin, Y.; Li, S.; Qian, Y.; Zhu, W.; Yuan, H.; Jiang, P.; Guo, R.; Wang, L. High-Entropy Alloys as a Platform for Catalysis: Progress, Challenges, and Opportunities. *ACS Catal.* **2020**, *10*, 11280–11306.
- (13) Duchesne, P. N.; Li, Z. Y.; Deming, C. P.; Fung, V.; Zhao, X.; Yuan, J.; Regier, T.; Aldalbahi, A.; Almarhoon, Z.; Chen, S.; Jiang, D. en; Zheng, N.; Zhang, P. Golden Single-Atomic-Site Platinum Electrocatalysts. *Nat. Mater.* **2018**, *17*, 1033–1039.
- (14) Firstov, G.; Timoshevskii, A.; Kosorukova, T.; Koval, Y.; Matviychuk, Y.; Verhovlyuk, P. Electronic and Crystal Structure of the High Entropy TiZrHfCoNiCu Intermetallics Undergoing Martensitic Transformation. *MATEC Web Conf.* **2015**, *33*, 6006.
- (15) Zhou, N.; Jiang, S.; Huang, T.; Qin, M.; Hu, T.; Luo, J. Single-Phase High-Entropy Intermetallic Compounds (HEICs): Bridging High-Entropy Alloys and Ceramics. *Sci. Bull.* **2019**, *64*, 856–864.
- (16) Yao, K.; Liu, L.; Ren, J.; Guo, Y.; Liu, Y.; Cao, Y.; Feng, R.; Wu, F.; Qi, J.; Luo, J.; Liaw, P. K.; Chen, W. High-Entropy Intermetallic Compound with Ultra-High Strength and Thermal Stability. *Scr. Mater.* **2021**, *194*, 113674.
- (17) Jia, Z.; Yang, T.; Sun, L.; Zhao, Y.; Li, W.; Luan, J.; Lyu, F.; Zhang, L. C.; Kružić, J. J.; Kai, J. J.; Huang, J. C.; Lu, J.; Liu, C. T. A Novel Multinary Intermetallic as an Active Electrocatalyst for Hydrogen Evolution. *Adv. Mater.* **2020**, *32*, 2000385.
- (18) Kosorukova, T. A.; Gerstein, G.; Odnosum, V. V.; Koval, Y. N.; Maier, H. J.; Firstov, G. S. Microstructure Formation in Cast TiZrHfCoNiCu and CoNiCuAlGaIn High Entropy Shape Memory Alloys: A Comparison. *Materials* **2019**, *12*, 4227.
- (19) Jung, W. G.; Kleppa, O. J. Standard Molar Enthalpies of Formation of Hf_3Ge_2 , $MeGe$ ($Me = Ir, Pt$) and Pt_2Ge . *J. Alloys Compd.* **1991**, *176*, 301–308.
- (20) He, J. Y.; Wang, H.; Huang, H. L.; Xu, X. D.; Chen, M. W.; Wu, Y.; Liu, X. J.; Nieh, T. G.; An, K.; Lu, Z. P. A Precipitation-Hardened High-Entropy Alloy with Outstanding Tensile Properties. *Acta Mater.* **2016**, *102*, 187–196.
- (21) Joseph, J.; Stanford, N.; Hodgson, P.; Fabijanic, D. M. Understanding the Mechanical Behaviour and the Large Strength/Ductility Differences between FCC and BCC $Al_xCoCrFeNi$ High Entropy Alloys. *J. Alloys Compd.* **2017**, *726*, 885–895.
- (22) Vikram, R. J.; Murty, B. S.; Fabijanic, D.; Suwas, S. Insights into Micro-Mechanical Response and Texture of the Additively Manufactured Eutectic High Entropy Alloy $AlCoCrFeNi_{2.1}$. *J. Alloys Compd.* **2020**, *827*, 154034.
- (23) Zaera, F. Probing Catalytic Reactions at Surfaces. *Prog. Surf. Sci.* **2001**, *69*, 1.
- (24) Ding, K.; Gulec, A.; Johnson, A. M.; Schweitzer, N. M.; Stucky, G. D.; Marks, L. D.; Stair, P. C. Identification of Active Sites in CO Oxidation and Water-Gas Shift over Supported Pt Catalysts. *Science* **2015**, *350*, 189–192.
- (25) Komatsu, T.; Sou, K.; Ozawa, K. Preparation and Catalytic Properties of Fine Particles of Pt-Ge Intermetallic Compound Formed inside the Mesopores of MCM-41. *J. Mol. Catal. A: Chem.* **2010**, *319*, 71–77.
- (26) Zheng, X.; Lin, H.; Zheng, J.; Duan, X.; Yuan, Y. Lanthanum Oxide-Modified Cu/SiO₂ as a High-Performance Catalyst for Chemoselective Hydrogenation of Dimethyl Oxalate to Ethylene Glycol. *ACS Catal.* **2013**, *3*, 2738–2749.
- (27) Dees, M. J.; Shido, T.; Iwasawa, Y.; Ponec, V. Infrared Studies of CO Adsorbed on Supported PtCo Catalysts. *J. Catal.* **1990**, *124*, 530–540.
- (28) Bouwman, R.; Biloen, P. Valence State and Interaction of Platinum and Germanium on Y-Al₂O₃ Investigated by X-Ray Photoelectron Spectroscopy. *J. Catal.* **1977**, *48*, 209–216.
- (29) Rimaz, S.; Chen, C.; Kawi, S.; Borgna, A. Promoting Effect of Ge on Pt-Based Catalysts for Dehydrogenation of Propane to Propylene. *Appl. Catal., A* **2019**, *588*, 117266.
- (30) Liu, W. E.; Mohney, S. E. Condensed Phase Equilibria in Transition Metal-Ga-Sb Systems and Predictions for Thermally Stable Contacts to GaSb. *J. Electron. Mater.* **2003**, *32*, 1090–1099.
- (31) Nakaya, Y.; Xing, F.; Ham, H.; Shimizu, K.; Furukawa, S. Doubly Decorated Platinum–Gallium Intermetallics as Stable Catalysts for Propane Dehydrogenation. *Angew. Chem., Int. Ed.* **2021**, *60*, 19715–19719.
- (32) Qi, L.; Babucci, M.; Zhang, Y.; Lund, A.; Liu, L.; Li, J.; Chen, Y.; Hoffman, A. S.; Bare, S. R.; Han, Y.; Gates, B. C.; Bell, A. T. Propane Dehydrogenation Catalyzed by Isolated Pt Atoms in $\equiv SiOZn-OH$ Nests in Dealuminated Zeolite Beta. *J. Am. Chem. Soc.* **2021**, *143*, 21364–21378.
- (33) Nakaya, Y.; Hirayama, J.; Yamazoe, S.; Shimizu, K.; Furukawa, S. Single-Atom Pt in Intermetallics as an Ultrastable and Selective Catalyst for Propane Dehydrogenation. *Nat. Commun.* **2020**, *11*, 2838.
- (34) Zha, S.; Sun, G.; Wu, T.; Zhao, J.; Zhao, Z. J.; Gong, J. Identification of Pt-Based Catalysts for Propane Dehydrogenation: Via a Probability Analysis. *Chem. Sci.* **2018**, *9*, 3925–3931.
- (35) Takamoto, S.; Shinagawa, C.; Motoki, D.; Nakago, K.; Li, W.; Kurata, I.; Watanabe, T.; Yayama, Y.; Iriuchi, H.; Asano, Y.; Onodera, T.; Ishii, T.; Kudo, T.; Ono, H.; Sawada, R.; Ishitani, R.; Ong, M.; Yamaguchi, T.; Kataoka, T.; Hayashi, A.; Charoenphakdee,

- N.; Ibuka, T. Towards Universal Neural Network Potential for Material Discovery Applicable to Arbitrary Combination of 45 Elements. *Nat. Commun.* **2022**, *13*, 2991.
- (36) Nakata, A.; Bowler, D. R.; Miyazaki, T. Optimized Multi-Site Local Orbitals in the Large-Scale DFT Program CONQUEST. *Phys. Chem. Chem. Phys.* **2015**, *17*, 31427–31433.
- (37) Romero-Muñiz, C.; Nakata, A.; Pou, P.; Bowler, D. R.; Miyazaki, T.; Pérez, R. High-Accuracy Large-Scale DFT Calculations Using Localized Orbitals in Complex Electronic Systems: The Case of Graphene-Metal Interfaces. *J. Phys. Condens. Matter* **2018**, *30*, 505901.
- (38) Nanba, Y.; Koyama, M. Thermodynamic Stability of Pd-Ru Alloy Nanoparticles: Combination of Density Functional Theory Calculations, Supervised Learning, and Wang-Landau Sampling. *Phys. Chem. Chem. Phys.* **2022**, *24*, 15452–15461.
- (39) Huerta, G. V.; Nanba, Y.; Kurata, I.; Nakago, K.; Takamoto, S.; Shinagawa, C.; Koyama, M. Calculations of Real-System Nanoparticles Using Universal Neural Network Potential PFP. **2021**, arXiv:2107.00963. DOI: [10.1039/D2CP01848A](https://doi.org/10.1039/D2CP01848A).
- (40) Nakaya, Y.; Miyazaki, M.; Yamazoe, S.; Shimizu, K.; Furukawa, S. Active, Selective, and Durable Catalyst for Alkane Dehydrogenation Based on a Well-Designed Trimetallic Alloy. *ACS Catal.* **2020**, *10*, 5163–5172.
- (41) Ravel, B.; Newville, M. ATHENA; ARTEMIS, HEPHAESTUS Data Analysis for X-Ray Absorption Spectroscopy Using IFEFFIT. *J. Synchrotron Radiat.* **2005**, *12*, 537–541.
- (42) Ankudinov, A.; Ravel, B.; Rehr, J. J.; Conradson, S. D. Real-Space Multiple-Scattering Calculation and Interpretation of x-Ray-Absorption near-Edge Structure. *Phys. Rev. B: Condens. Matter Mater. Phys.* **1998**, *58*, 7565–7576.
- (43) Segall, M. D.; Lindan, P. J. D.; Probert, M. J.; Pickard, C. J.; Hasnip, P. J.; Clark, S. J.; Payne, M. C. First-Principles Simulation: Ideas, Illustrations and the CASTEP Code. *J. Phys. Condens. Matter* **2002**, *14*, 2717–2744.
- (44) Hammer, B.; Hansen, L. B.; Nørskov, J. K. Improved Adsorption Energetics within Density-Functional Theory Using Revised Perdew-Burke-Ernzerhof Functionals. *Phys. Rev. B: Condens. Matter Mater. Phys.* **1999**, *59*, 7413–7421.
- (45) Tkatchenko, A.; Scheffler, M. Accurate Molecular van Der Waals Interactions from Ground-State Electron Density and Free-Atom Reference Data. *Phys. Rev. Lett.* **2009**, *102*, 073005.
- (46) Hu, K.; Wu, M.; Hinokuma, S.; Ohto, T.; Wakisaka, M.; Fujita, J. I.; Ito, Y. Boosting Electrochemical Water Splitting: Via Ternary NiMoCo Hybrid Nanowire Arrays. *J. Mater. Chem. A* **2019**, *7*, 2156–2164.
- (47) Halgren, T. A.; Lipscomb, W. N. The Synchronous-Transit Method for Determining Reaction Pathways and Locating Molecular Transition States. *Chem. Phys. Lett.* **1977**, *49*, 225–232.
- (48) Govind, N.; Petersen, M.; Fitzgerald, G.; King-Smith, D.; Andzelm, J. A Generalized Synchronous Transit Method for Transition State Location. *Comput. Mater. Sci.* **2003**, *28*, 250–258.

■ NOTE ADDED AFTER ASAP PUBLICATION

This paper was published on August 19, 2022. Scheme 1 has been updated and the revised version posted on August 24, 2022.

□ Recommended by ACS

A Priori Design of Dual-Atom Alloy Sites and Experimental Demonstration of Ethanol Dehydrogenation and Dehydration on PtCrAg

Paul L. Kress, Matthew M. Montemore, *et al.*

MARCH 08, 2023

JOURNAL OF THE AMERICAN CHEMICAL SOCIETY

[READ ▾](#)

Interstitial Carbon Dopant in Palladium–Gold Alloy Boosting the Catalytic Performance in Vinyl Acetate Monomer Synthesis

Yuki Nakaya, Shinya Furukawa, *et al.*

JANUARY 24, 2023

JOURNAL OF THE AMERICAN CHEMICAL SOCIETY

[READ ▾](#)

Role of Fluxionality and Metastable Isomers in the ORR Activity: A Case Study

Rahul Kumar Sharma, Biswarup Pathak, *et al.*

JANUARY 02, 2023

THE JOURNAL OF PHYSICAL CHEMISTRY C

[READ ▾](#)

Atomic Structural Origin of the High Methanol Selectivity over In_2O_3 -Metal Interfaces: Metal–Support Interactions and the Formation of a InO_x Overlayer in Ru/ In_2O_3 Cata...

Ning Rui, José A. Rodriguez, *et al.*

FEBRUARY 17, 2023

ACS CATALYSIS

[READ ▾](#)

[Get More Suggestions >](#)